

ARTICLE OPEN



Giant anomalous Hall and Nernst effect in magnetic cubic Heusler compounds

Jonathan Noky¹, Yang Zhang^{1,2}, Johannes Gooth¹, Claudia Felser¹ and Yan Sun¹✉

The interplay of magnetism and topology opens up the possibility for exotic linear response effects, such as the anomalous Hall effect and the anomalous Nernst effect, which can be strongly enhanced by designing a large Berry curvature in the electronic structure. Magnetic Heusler compounds are a promising class of materials for this purpose because they are versatile, show magnetism, and their electronic structure hosts strong topological features. Here, we provide a comprehensive study of the intrinsic anomalous transport for magnetic cubic full Heusler compounds and we illustrate that several Heusler compounds outperform the best so far reported materials. The results reveal the importance of symmetries, especially mirror planes, in combination with magnetism for giant anomalous Hall and Nernst effects, which should be valid in general for linear responses (spin Hall effect, spin orbital torque, etc.) dominated by intrinsic contributions.

npj Computational Materials (2020)6:77; <https://doi.org/10.1038/s41524-020-0342-5>

INTRODUCTION

In recent years a huge effort has been put in identifying topological phases of matter in real materials, culminating in a way to classify all materials via elementary band representation theory^{1–4}. However, until now this is done specifically for time-reversal symmetric, i.e., non-magnetic materials. For the investigation of magnetic materials the only possibility is to perform systematic calculations for each single compound which has been done for selected material classes^{5–15}. The restriction to time-reversal symmetric systems excludes not only a large number of compounds but also all kinds of properties that require broken time-reversal symmetry. Specifically, in magnetic materials there exist linear response effects that are not possible in time-reversal symmetric systems: There is the anomalous Hall effect (AHE)^{16,17}, which describes the transverse voltage drop that results from an applied longitudinal current, and the anomalous Nernst effect (ANE)^{18,19}, which is analogous to the AHE but with a longitudinal temperature gradient instead of a current.

A promising class of candidate materials is the magnetic Heusler compounds²⁰. They are a versatile group of materials that are easily tunable for many different properties^{21–25}. Heusler compounds host both magnetism and topological band structures, leading to a very large Berry curvature (BC). A strong AHE and the highest so far reported ANE were found in a Heusler system, Co₂MnGa^{26–31}. This renders them as a promising platform for investigating the anomalous linear response effects like the AHE, the ANE, and the magneto-optic Kerr effect^{32–34} (MOKE), all of these have their intrinsic contributions enhanced due to the BC^{17,19,35,36}.

Studying these effects gives insights into the electrical, thermoelectrical, and magneto-optical properties of magnetic materials³⁷ and can also be utilized in applications, e.g., for data storage, data transfer, and thermoelectric power generation. Therefore, both the understanding of the underlying mechanisms and the search for materials with strong linear responses in the effects described above has attracted extensive interest in both fundamental physics and material science. However, the plethora of possible compounds also makes it challenging to figure out the

most promising ones. Therefore, simple guidelines for estimates of the linear responses are required to open up new possibilities in the search for interesting materials with large linear response effects.

RESULTS AND DISCUSSION

Guiding principles for large AHE and ANE

In this work we theoretically investigate all cubic and stable magnetic full Heusler compounds from the Heusler database of the University of Alabama³⁸. This is done by applying the workflow shown in Fig. 1 to all compounds which satisfy the above mentioned criteria. We link the resulting anomalous Hall conductivity (AHC), anomalous Nernst conductivity (ANC), and Kerr angle to structural and electronic properties of the materials, such as space group (SG), lattice constant, magnetic moment, number of valence electrons, and density of states at the Fermi level.

To reveal general rules for the linear response in cubic Heusler compounds, we analyzed these results carefully for underlying concepts and correlations. A distinct difference is present between the two space groups. In Fig. 2a and b the crystal structure of a regular (SG 225) and an inverse (SG 216) cubic Heusler compound are shown, respectively. As the main difference between the two groups, SG 225 hosts three mirror planes at $x = 0$, $y = 0$, and $z = 0$ that are not present in SG 216 due to the reduced symmetry. Comparing now the values for the AHC, ANC, and Kerr angle of both space groups, we find larger values of all three properties for the regular structure (SG 225), as shown in Fig. 2d–f.

For an understanding of the underlying mechanism of this difference, the presence of mirror planes plays a crucial role. To elaborate on the influence of this specific symmetry, we analyze a simple four-band model proposed by Rauch et al.³⁹

$$\begin{aligned}
 H = & (m - 6M + 2(\cos k_x + \cos k_y + \cos k_z))\tau_z \otimes \sigma_0 \\
 & + B\tau_z \otimes \sigma_z + c \sin k_z \tau_x \otimes \sigma_z \\
 & + c \sin k_x \tau_x \otimes \sigma_x + c \sin k_y \tau_x \otimes \sigma_y.
 \end{aligned}
 \tag{1}$$

¹Max Planck Institute for Chemical Physics of Solids, D-01187 Dresden, Germany. ²Massachusetts Institute of Technology, Cambridge, MA 02139, USA. ✉email: ysun@cpfs.mpg.de

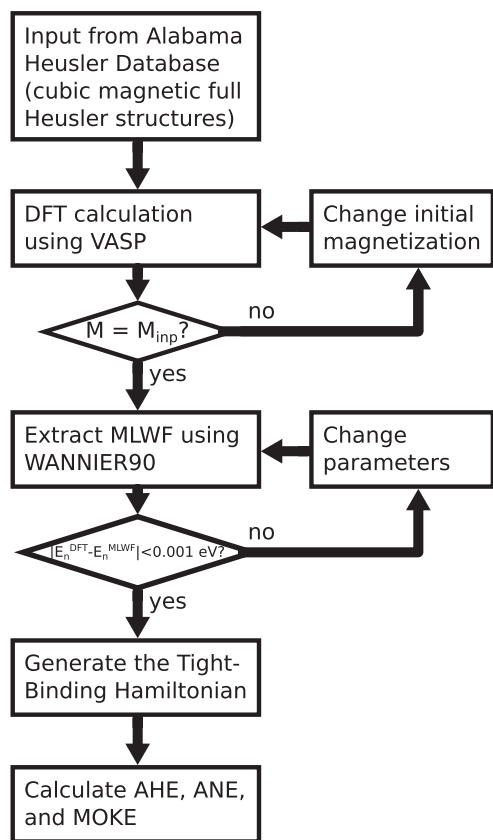


Fig. 1 Workflow for the analysis of the materials. All stable, cubic, and magnetic full Heusler structures from the Alabama Heusler Database³⁸ are taken as a starting input. The parameters to control the MLWF generation include the orbital projection and the inner and outer energy window for the disentanglement.

For $m = M = c = 1$ eV and $B = 2$ eV this model possesses a mirror in the k_x - k_y -plane, that hosts a nodal line (NL) at the Fermi level protected from this symmetry (Fig. 3a left panel). We now introduce a term for spin-orbit coupling (SOC), that can be interpreted as a consequence of a magnetization along the x -direction^{40,41}

$$H^{\text{SOC}} = \lambda c (\sin k_x \tau_x \otimes \sigma_x + \sin k_z \tau_x \otimes \sigma_y) \quad \text{with } \lambda = 0.01 \quad (2)$$

Because a magnetization along the x -direction in combination with SOC breaks the mirror symmetry in the k_x - k_y plane, the NL is no longer protected and gets gapped. The created gap is an inverted band gap that induces strong BC into the band structure. The distribution of the BC in the Brillouin zone is focused only around the former NL, as shown in Fig. 3a right panel. Consequently, the now gapped system exhibits a large AHE and ANE around the Fermi level.

From this model the larger linear response values in the materials of SG 225 can be understood. Because SG 225 hosts three mirror planes perpendicular to each other, there are three NLs protected by these symmetries. However, all the investigated compounds are magnetic, therefore depending on the magnetization direction the mirror symmetries are broken and the NLs are no longer protected (see Fig. 2c for a magnetization along (001)). Consequently, the respective NLs gap out and induce large BC into the band structure⁴⁰⁻⁴². This effect leads to the enhanced values in AHC, ANC, and the Kerr angle, as they are closely related to the BC (see Methods section and Supplementary Fig. 1).

It is also interesting to investigate the connection between the number of valence electrons and the AHC/ANC. Figure 4a reveals a double peak structure in the AHC with a small maximum located

at 21 valence electrons and a larger maximum at 28. This can be seen for both maximum values (light green area) and average values (blue line). A similar behavior of a double peak structure with a minimum around 23–24 valence electrons (gray area) exists for the ANC in Fig. 4b. Due to the fact that both AHE and ANE are very sensitive to the Fermi level E_F we also investigate the maximum AHC and ANC in a range of 250 meV around E_F . Scanning a range of possible Fermi energies is especially interesting because Heusler compounds are easy to dope and thus the Fermi level can be controlled by changing the compositions slightly. Figure 4c and d shows the dependence of maximum AHC and ANC, respectively, on the number of valence electrons. Also here the double peak structure with the same minimum position can be identified.

This behavior can be understood when taking the energetic position of the BC inducing features into account. Because the valence electron count can be related to the filling of the band structure, certain electron numbers move E_F close to the topological features while at other fillings there is no strong BC at E_F . A valence electron count of 21 or 28 corresponds to a filling level with the topological features close to E_F , which leads in consequence to large AHC and ANC.

Another interesting connection to investigate is between the different responses. Looking at the dependence of the ANC on the AHC in Fig. 4e it can be seen that the two properties are independent of each other, i.e., a large AHC not necessarily causes a large ANC. This shows the importance of treating the two mechanisms independently even if they are both linked to the BC⁴⁰. However, a different picture arises when taking the maximum value of both AHC and ANC in a range of 250 meV around E_F into account, as shown in Fig. 4f. Here, a linear connection between the absolute values is visible. This can be understood from the fact that both effects rely on a large BC in the band structure. Due to the different mechanisms of the two effects (see Methods section) the energetic distribution of the contributions is different but nonetheless the presence of large BC increases both of these values^{40,41}.

In conclusion, the statistical analysis we performed in the previous paragraphs shows, that the symmetry of the compound is very important to find materials with large linear responses. We find that mirror symmetries in combination with magnetism are crucial for getting strong effects. Apart from that the most important influence is the exact location of the BC in the band structure with respect to the Fermi level. For full Heusler compounds our calculations reveal that this is the case for a number of valence electrons around 21 and 28. We do not find such clear correlations for the Kerr angle because it is sensitive not only to the Fermi level position but to the transition energy $\hbar\omega$.

In addition to these general results, the calculations for the single materials show very appealing properties. In particular, some of the calculated values are in range of or even exceed the highest so far reported values.

Selected materials with large AHE and ANE

In the following we present selected results of the calculated compounds. The full results for the 255 compounds are shown in the Supplementary Information. Table 1 shows materials with a large AHC and/or ANC.

Looking at the AHC we find that the compounds Co_2MnAl , Rh_2MnAl , and Rh_2MnGa have values almost as large as Fe^{43} , which is the highest value ever reported. This is especially interesting because the first two mentioned compounds have already been synthesized^{44,45}. For the ANC the largest reported experimental value so far is $6 \text{ A m}^{-1} \text{ K}^{-1}$ in $\text{Co}_2\text{MnGa}^{28,29}$. It is important to note that this value is not reached at the charge neutral point but with some doping²⁸. In the Heusler compounds we find a similar value

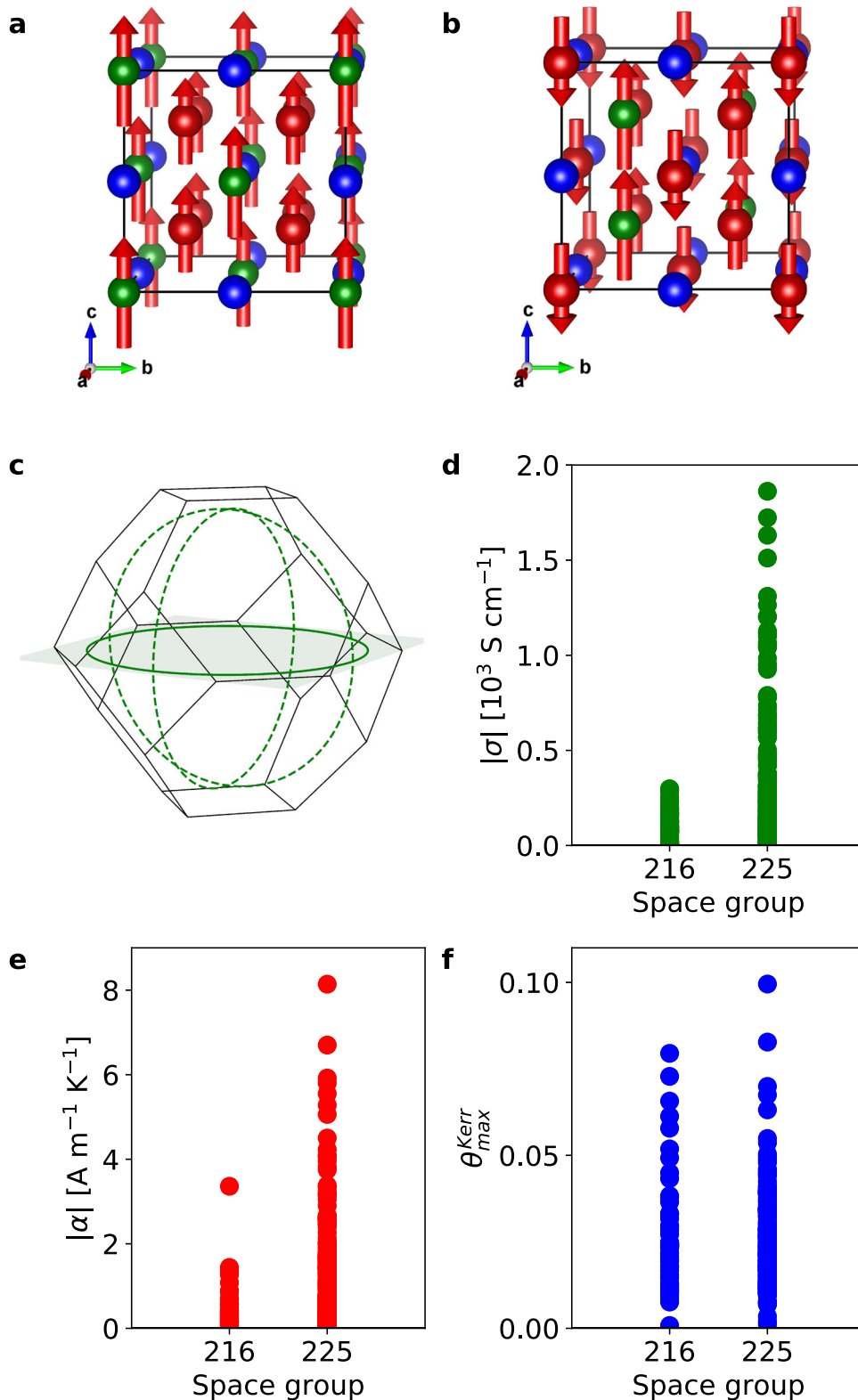


Fig. 2 Comparison of the different space groups. **a, b** Crystal structure of the regular (space group 225) and inverse (space group 216) Heusler structure, respectively. **c** Brillouin zone of the cubic Heusler compounds. The green lines represent the nodal lines which are enforced by symmetry in the regular compounds. When choosing the magnetic moments aligned along (001), only the horizontal mirror plane (green) is preserved. Consequently, the dashed nodal lines gap out. **d** Anomalous Hall conductivity (AHC), σ , **e** anomalous Nernst conductivity (ANC), α , and **f** maximum Kerr angle, $\theta_{\max}^{\text{Kerr}}$, in a range from 1 to 4 eV in dependence of the space group. Space group 225 shows the larger values for all three responses.

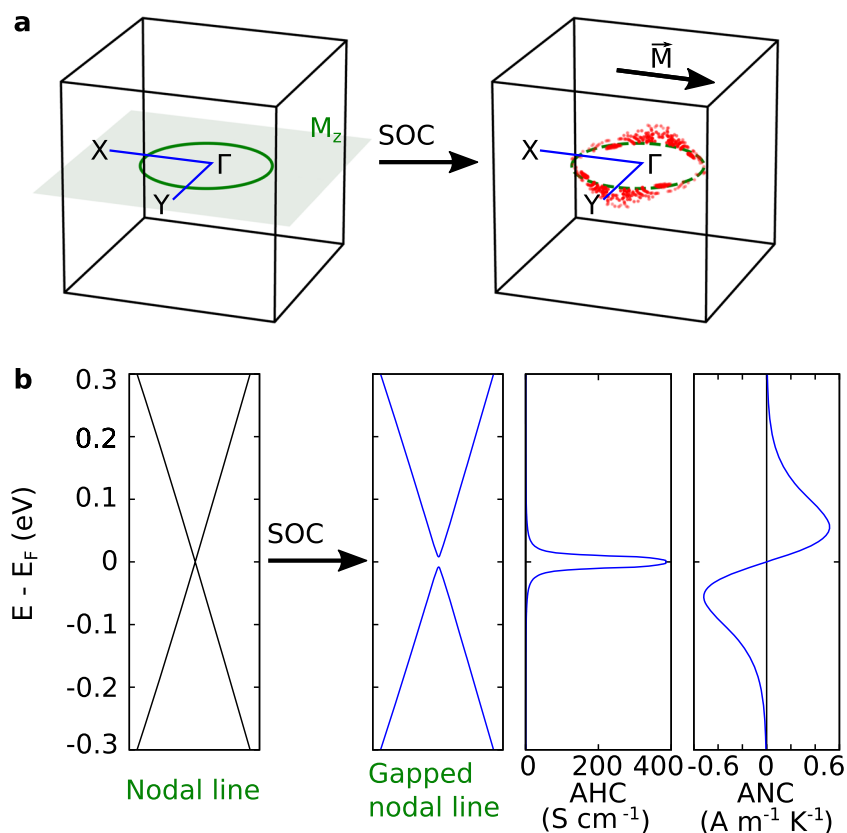


Fig. 3 Nodal line model system. **a** Left panel: System without spin–orbit coupling. The mirror symmetry of the model protects a nodal line in the k_x – k_y plane. Right panel: Introducing spin–orbit coupling breaks the mirror symmetry and gaps out the nodal line, inducing large Berry curvature (red dots) around the former nodal line. **b** Band structures of the systems without and with spin–orbit coupling, respectively. The gapped nodal line creates large anomalous Hall and Nernst effects.

for Rh_2NiSi and an even larger value for Rh_2NiSn , which has already been synthesized⁴⁶.

However, it is important to also include the energy dependence of the AHC and ANC to account for energetic shifts away from the charge neutral point. Therefore, we additionally show the largest possible value in a range of 250 meV around E_F in Table 1. This is, because real materials will always have some vacancies or defects which lead to small doping effects and consequently to a shift in the Fermi level. Furthermore, Heusler compounds can also be doped in a controlled way to engineer a compound with the desired Fermi level position. Taking the possibility of doping into account, all compounds shown in Table 1 have a very large ANC, with most of them even exceeding the current record value. The largest values that we find are $10.99 \text{ A m}^{-1} \text{ K}^{-1}$ in Co_2FeSn , $9.11 \text{ A m}^{-1} \text{ K}^{-1}$ in Co_2FeGe , and $8.33 \text{ A m}^{-1} \text{ K}^{-1}$ in Rh_2MnGa .

These results show that the changes in E_F can have a large influence on the anomalous transport coefficients, especially on the ANC. To illustrate this more in detail, Fig. 5 shows two example materials from Table 1 with the energy-dependent AHC and ANC. In both band structures in Fig. 5 the effect shown in the tight-binding model of the NL can be seen: For the calculation without SOC there is a band crossing along the W – Γ line, which gets gapped by the introduction of SOC. It is important to note that the corresponding NLs also have dispersion in energy, which is the reason that the peak in the AHC does not coincide with the crossing along the W – Γ line.

For the AHC a small shift in the Fermi level can greatly enhance or decrease the value, as it can be seen for Rh_2NiSn (Fig. 5 upper panel): Here the AHC is 1682 S cm^{-1} for $E - E_F = -110 \text{ meV}$ but only 360 S cm^{-1} at E_F . However, for the ANC these changes are even stronger. This can be seen in Rh_2MnGa (Fig. 5 lower panel),

where a change from E_F to $E - E_F = -130 \text{ meV}$ leads to a change in the ANC from 3.82 to $-8.33 \text{ A m}^{-1} \text{ K}^{-1}$, including a sign change.

Therefore, it is very important for comparison between experimental and calculated results to take the exact position of the Fermi level into account. The energy dependence of the AHC and ANC for all calculated materials is given in the Supplementary Information.

There can be different sources of the BC in a band structure. Mainly, it can come from Weyl points (WP) that act as monopoles for the BC or from inverted band gaps, that are created from a gapped out NL in these compounds, when a mirror symmetry is broken via magnetization. While WPs are present in most of the Heusler compounds in this work, NLs are only possible in SG 225. Here, both mechanisms are present. To find out the dominating effect, one can look into the BC distribution in the Brillouin zone. In the case of WPs the distribution is mainly point-like, as it can be seen for Rh_2NiSn in Fig. 5. For the NL case, also the BC forms a line following the former NL like in Rh_2MnGa in Fig. 5. For the high-performance compounds in Table 1 the last column gives the dominating mechanism.

Summary

In summary, we have investigated the AHE, ANE, and MOKE of all the stable magnetic cubic full Heusler compounds given in the Heusler database of the University of Alabama³⁸. From evaluating the linear response values of the different space groups we find that the symmetries are very important. To achieve a large AHC and ANC the presence of mirror symmetries turns out to be crucial, which leads in combination with magnetism to a large BC in the band structure and consequently to large linear response coefficients. The existence of mirror planes should also be

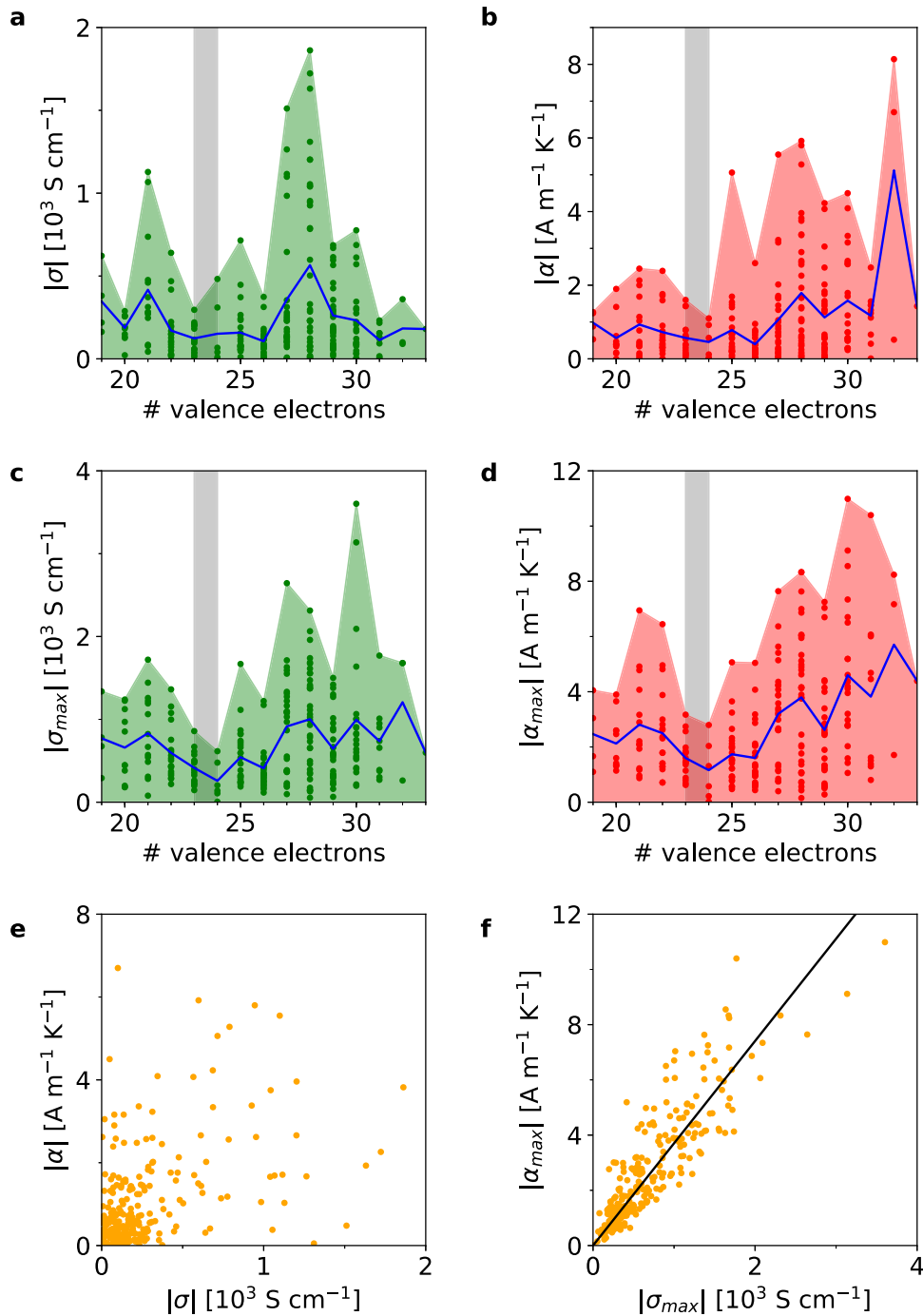


Fig. 4 Connections between the anomalous Hall conductivity (AHC) and the anomalous Nernst conductivity (ANC). **a** AHC, σ , and **b** ANC, α , in dependence of the number of valence electrons. **c** Maximum of σ and **d** α in a window of 250 meV around E_F in dependence of the number of valence electrons. The green/red area connects the maximum values for each valence electron count. The blue line shows the average value. The gray area is a guide to the eye for the minimum area at 23–24 valence electrons between the two peaks at 21 and 28 valence electrons. **e** α in dependence of σ . No correlation is visible. **f** Maximum of α in dependence of the maximum of σ . A clear linear connection can be seen.

important for other linear response effects that are dominated by intrinsic contributions such as the spin Hall effect, spin Nernst effect, and spin–orbit torque.

Apart from that the linear response is mostly influenced by the exact position of the BC in the band structure with respect to the Fermi level. For Heusler compounds, this can be linked to the number of valence electrons with two sweet spots at 21 and 28 electrons per unit cell. Some of the materials show a very large

AHC and/or ANC, which is close to or even exceeds the highest values that are reported so far. It is important to note, that both AHC and ANC are strongly dependent on the position of the Fermi level and therefore on the doping of the investigated material. This always has to be taken into account when comparing experimental and theoretical results.

This work shows the versatility and usability of Heusler compounds to achieve large linear response values and illustrates

Table 1. Results for selected materials with large anomalous Hall conductivity (AHC) and/or anomalous Nernst conductivity (ANC).

Material	SG	a_0 (Å)	μ (μ_B /f.u.)	AHC ($S\text{ cm}^{-1}$)	AHC $_{\text{max}}$ ($\Delta E/\Delta n$) ($S\text{ cm}^{-1}$)	ANC ($A\text{ m}^{-1}\text{ K}^{-1}$)	ANC $_{\text{max}}$ ($\Delta E/\Delta n$) ($A\text{ m}^{-1}\text{ K}^{-1}$)	Main BC source
Co ₂ CrAl	225	5.7	3.0	-313	-1089 (-0.04/-0.24)	3.23	3.23 (0.0/-0.03)	WP
Co ₂ MnAl	225	5.7	4.04	-1631	-1739 (-0.01/-0.02)	1.93	4.13 (0.04/0.05)	NL
Co ₂ MnGa	225	5.72	4.11	-1310	-1473 (0.05/0.1)	-0.05	4.79 (0.09/0.17)	NL
Co ₂ FeSi	225	5.63	5.4	-275	2092 (0.12/0.8)	2.57	7.34 (0.08/0.49)	WP
Co ₂ FeGe	225	5.74	5.57	-78	3136 (0.14/0.84)	3.16	9.11 (0.08/0.43)	NL
Co ₂ FeSn	225	5.99	5.6	49	3602 (0.12/0.85)	4.5	10.99 (0.07/0.4)	NL
Fe ₂ MnP	225	5.55	4.0	-1202	-1373 (-0.04/-0.13)	2.66	7.63 (0.12/0.37)	NL
Fe ₂ MnAs	225	5.7	4.02	-1043	-1413 (-0.06/-0.2)	3.75	7.0 (0.1/0.31)	NL
Fe ₂ MnSb	225	5.95	4.11	-1203	-1374 (-0.06/-0.31)	3.96	-6.02 (-0.12/-0.67)	NL
Rh ₂ MnAl	225	6.04	4.1	-1723	-2064 (-0.05/-0.13)	2.26	-6.06 (-0.12/-0.39)	NL
Rh ₂ MnGa	225	6.06	4.13	-1862	-2313 (-0.04/-0.13)	3.82	-8.33 (-0.13/-0.45)	NL
Rh ₂ FeIn	225	6.27	4.2	-18	1270 (0.12/0.63)	3.05	4.42 (0.07/0.33)	WP
Rh ₂ CoAl	225	5.98	3.03	345	1005 (0.05/0.26)	4.09	-4.2 (0.12/0.57)	NL
Rh ₂ NiSi	225	5.89	0.98	100	1678 (0.14/0.6)	6.7	7.17 (0.04/0.14)	WP
Rh ₂ NiSn	225	6.21	1.0	360	1680 (0.11/0.55)	8.14	8.24 (0.01/0.04)	WP
Ru ₂ MnP	225	5.91	3.95	-926	-1159 (0.03/0.08)	-3.38	-5.12 (-0.05/-0.15)	NL
Ru ₂ FeP	225	5.9	4.13	-686	-1300 (0.04/0.17)	-4.23	-4.37 (-0.01/-0.05)	WP
Ru ₂ FeAs	225	6.02	4.23	-566	-1378 (0.08/0.32)	-4.07	4.15 (0.16/0.74)	WP
Ru ₂ CoGe	225	5.96	1.99	-138	-1500 (0.15/0.91)	-2.48	-6.7 (0.11/0.68)	WP
Ru ₂ CoP	225	5.84	2.18	-776	-899 (-0.03/-0.14)	1.18	-6.5 (-0.12/-0.62)	NL

The full results are shown in the Supplementary Information. Listed are space group (SG), theoretical lattice constant (a_0), theoretical magnetic moment (μ), AHC, maximum AHC, ANC, maximum ANC. The maximum values are obtained in an energy window of 250 meV around the Fermi level. ΔE gives the energy distance in meV and Δn the electron difference of the maximum values with regard to the Fermi level. The last column gives the main source of Berry curvature (BC) as either Weyl points (WP) or gapped nodal lines (NL). Very large values for both AHC and ANC are possible.

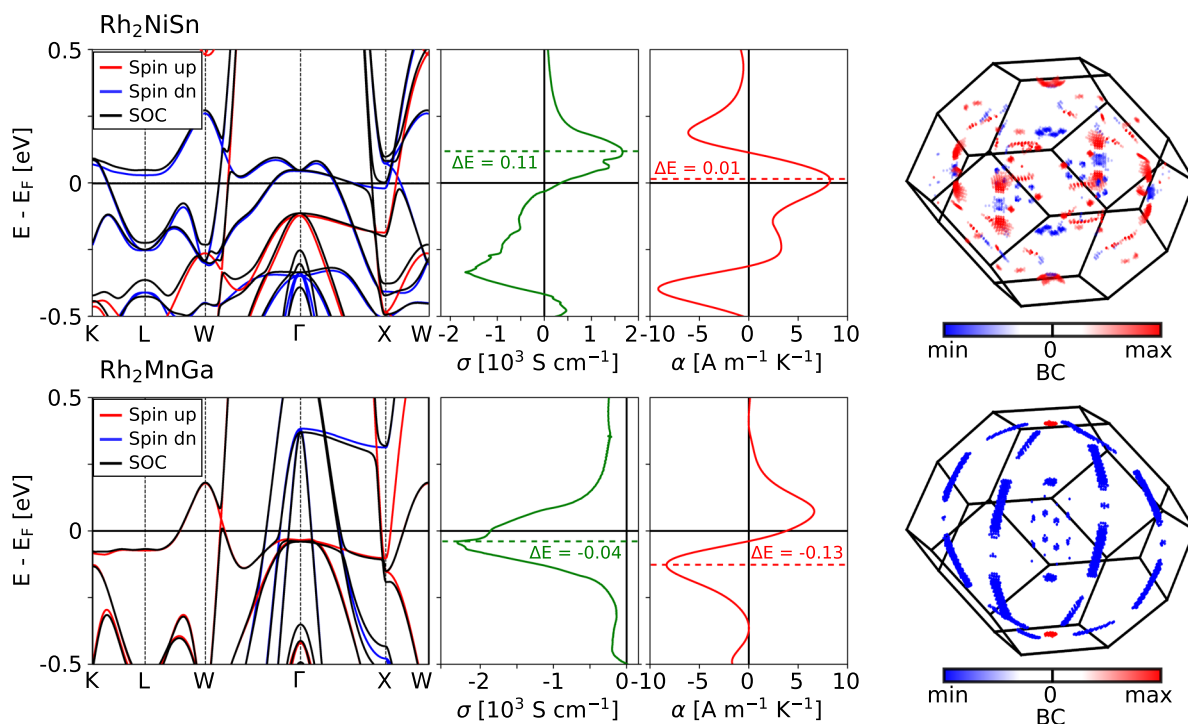


Fig. 5 Detailed results for selected materials. Band structure with and without spin-orbit coupling, anomalous Hall conductivity (AHC), σ , anomalous Nernst conductivity (ANC), α , and Berry curvature (BC) distribution in the Brillouin zone for Rh₂NiSn and Rh₂MnGa. Both AHC and ANC are strongly dependent on the position of the Fermi level. Note the scaling factor in the AHC. The nodal lines in Rh₂MnGa are clearly visible.

the importance of mirror symmetries. It proposes a comprehensive list of their properties including large values for the AHC and new record values for the ANC and thus paves the way for new high-performance compounds.

METHODS

Detailed description of the workflow

For our investigation we start with the structural data given by the Heusler Database of the University of Alabama³⁸ where we choose all cubic compounds that are given as stable. The compounds without a magnetization are set aside because for the investigated linear responses only systems without time-reversal symmetry are interesting. This results in 255 materials which satisfy these conditions.

For the chosen compounds we take the lattice constant and the space group as inputs for the density-functional theory (DFT) calculation. For this we employ the package VASP⁴⁷ with pseudopotentials, plane waves and the generalized-gradient approximation (GGA)⁴⁸ for the exchange-correlation potential. For full Heusler compounds previous works have shown good agreement between experimental results and theory on the GGA level^{25,28,29,49,50}. Therefore we focus on this level of approximation. For the self-consistent calculations a k mesh of $13 \times 13 \times 13$ points was used. The DFT calculation is done with different starting values for the magnetic moments until the total magnetization given in the database is reproduced. For all calculations the magnetic moments were chosen to be parallel to the (001) direction. Changing the magnetization direction changes the local Berry curvature distribution due to differently broken crystal symmetries. However, because of the cubic symmetries in the full Heusler compounds the integral value resulting in the anomalous transport coefficients does not change (see also Supplementary Fig. 2). In the following we create Wannier functions via the package Wannier90⁵¹ with a projection of the Bloch states to the atomic orbitals. The wannierization is repeated with different parameters (such as orbital projections and both inner and outer energy windows) until the average energy difference between the Wannier functions and the DFT wave functions along the path $K-L-W-\Gamma-X-W-\Gamma-U$ in k space is <1 meV in a range from $E_F - 4$ eV to $E_F + 4$ eV. Then we extract Tight-Binding parameters and use this Hamiltonian, H , to calculate the Berry curvature (BC), Ω , via the Kubo formalism^{17,35,36}

$$\Omega_{ij}^n = \sum_{m \neq n} \frac{\langle n | \frac{\partial H}{\partial k_i} | m \rangle \langle m | \frac{\partial H}{\partial k_j} | n \rangle - (i \leftrightarrow j)}{(E_n - E_m)^2}, \quad (3)$$

with $|n\rangle$ and E_n being the eigenstates and -energies of H , respectively.

We evaluate the anomalous Hall conductivity (AHC), σ , from the BC as

$$\sigma_{ij} = \frac{e^2}{h} \sum_n \int \frac{d^3k}{(2\pi)^3} \Omega_{ij}^n f_n \quad (4)$$

and the anomalous Nernst conductivity (ANC), α , as proposed by Xiao et al.^{19,36}

$$\alpha_{ij} = -\frac{1}{T} \frac{e}{h} \sum_n \int \frac{d^3k}{(2\pi)^3} \Omega_{ij}^n \left[(E_n - E_F) f_n + k_B T \ln \left(1 + \exp \frac{E_n - E_F}{-k_B T} \right) \right]. \quad (5)$$

Here, T is the actual temperature, f_n is the Fermi distribution, and E_F is the Fermi level.

Furthermore, we calculate the optical Hall conductivity, $\sigma(\omega)$, using the Kubo formalism^{52,53}:

$$\sigma_{ij}(\omega) = \frac{e^2}{h} \sum_{n \neq m} \int \frac{d^3k}{(2\pi)^3} (f_{n,k} - f_{m,k}) \times \frac{\langle n | \frac{\partial H}{\partial k_i} | m \rangle \langle m | \frac{\partial H}{\partial k_j} | n \rangle - (i \leftrightarrow j)}{(E_n - E_m)^2 - (\hbar\omega + i\delta)^2}, \quad (6)$$

where ω is the transition energy and δ has a positive infinitesimal value. From this we evaluate the Kerr angle, θ_K , as^{33,34}

$$\theta_K + i\eta_K = \frac{-\sigma_{xy}}{\sigma_{xx} \sqrt{1 + \frac{4\eta_i}{\omega} \sigma_{xx}}}. \quad (7)$$

DATA AVAILABILITY

All data generated and/or analyzed during this study are included in this article and its Supplementary Information file. The data are available from the corresponding author upon reasonable request.

CODE AVAILABILITY

All code used to calculate the presented results is available from the corresponding author upon reasonable request.

Received: 3 February 2020; Accepted: 11 May 2020;

Published online: 05 June 2020

REFERENCES

- Bradlyn, B. et al. Topological quantum chemistry. *Nature* **547**, 298–305 (2017).
- Cano, J. et al. Topology of disconnected elementary band representations. *Phys. Rev. Lett.* **120**, 266401 (2018).
- Cano, J. et al. Building blocks of topological quantum chemistry: elementary band representations. *Phys. Rev. B* **97**, 35139 (2018).
- Vergniory, M. G. et al. A complete catalogue of high-quality topological materials. *Nature* **566**, 480–485 (2019).
- Wang, Z. et al. Time-reversal-breaking Weyl fermions in magnetic Heusler alloys. *Phys. Rev. Lett.* **117**, 236401 (2016).
- Wang, H., Luo, W. & Xiang, H. Prediction of high-temperature quantum anomalous Hall effect in two-dimensional transition-metal oxides. *Phys. Rev. B* **95**, 125430 (2017).
- Wang, R. et al. Nodal line fermions in magnetic oxides. *Phys. Rev. B* **97**, 241111 (2018).
- Wang, R. et al. Ferromagnetic Weyl fermions in CrO_2 . *Phys. Rev. B* **97**, 195157 (2018).
- Jin, Y., Wang, R., Xia, B., Zheng, B. & Xu, H. Three-dimensional quantum anomalous Hall effect in ferromagnetic insulators. *Phys. Rev. B* **98**, 081101 (2018).
- Xia, B. et al. Robust twin pairs of Weyl fermions in ferromagnetic oxides. *Phys. Rev. Lett.* **122**, 057205 (2019).
- Liu, D. et al. Magnetic Weyl semimetal phase in a Kagomé crystal. *Science* **365**, 1282–1285 (2019).
- Morali, N. et al. Fermi-arc diversity on surface terminations of the magnetic Weyl semimetal $\text{Co}_3\text{Sn}_2\text{S}_2$. *Science* **365**, 1286–1291 (2019).
- Gao, Q., Opahle, I. & Zhang, H. High-throughput screening for spin-gapless semiconductors in quaternary Heusler compounds. *Phys. Rev. Mater.* **3**, 024410 (2019).
- Olsen, T. et al. Discovering two-dimensional topological insulators from high-throughput computations. *Phys. Rev. Mater.* **3**, 024005 (2019).
- Sanvito, S. et al. Accelerated discovery of new magnets in the heusler alloy family. *Sci. Adv.* **3**, e1602241 (2017).
- Pugh, E. M. & Rostoker, N. Hall effect in ferromagnetic materials. *Rev. Modern Phys.* **25**, 151–157 (1953).
- Nagaosa, N., Sinova, J., Onoda, S., MacDonald, A. H. & Ong, N. P. Anomalous Hall effect. *Rev. Modern Phys.* **82**, 1539–1592 (2010).
- Nernst, W. Ueber die electromotorischen Kräfte, welche durch den Magnetismus in von einem Wärmestrome durchflossenen Metallplatten geweckt werden. *Ann. Phys.* **267**, 760–789 (1887).
- Xiao, D., Yao, Y., Fang, Z. & Niu, Q. Berry-phase effect in anomalous thermoelectric transport. *Phys. Rev. Lett.* **97**, 026603 (2006).
- Heusler, F. Über magnetische Manganlegierungen. *Verh. Deutsch. Phys. Ges.* **5**, 219 (1903).
- Chadov, S. et al. Tunable multifunctional topological insulators in ternary Heusler compounds. *Nat. Mater.* **9**, 541–545 (2010).
- Hirschberger, M. et al. The chiral anomaly and thermopower of Weyl fermions in the half-Heusler GdPtBi . *Nat. Mater.* **15**, 1161–1165 (2016).
- Wollmann, L., Nayak, A. K., Parkin, S. S. P. & Felser, C. Heusler 4.0: tunable materials. *Ann. Rev. Materials Res.* **47**, 247–270 (2016).
- Manna, K. et al. From colossal to zero: controlling the anomalous Hall effect in magnetic Heusler compounds via Berry curvature design. *Phys. Rev. X* **8**, 041045 (2018).
- Manna, K., Sun, Y., Muechler, L., Kübler, J. & Felser, C. Heusler, Weyl and Berry. *Nat. Rev. Mater.* **3**, 244–256 (2018).
- Belopolski, I. et al. Discovery of topological Weyl fermion lines and drum-head surface states in a room temperature magnet. *Science* **365**, 1278–1281 (2019).
- Ludbrook, B. M., Ruck, B. J. & Granville, S. Perpendicular magnetic anisotropy in Co_2MnGa and its anomalous Hall effect. *Appl. Phys. Lett.* **110**, 62408 (2017).
- Guin, S. N. et al. Anomalous Nernst effect beyond the magnetization scaling relation in the ferromagnetic Heusler compound Co_2MnGa . *NPG Asia Mater.* **11**, 16 (2019).
- Sakai, A. et al. Giant anomalous Nernst effect and quantum-critical scaling in a ferromagnetic semimetal. *Nat. Phys.* **14**, 1119–1124 (2018).
- Reichlova, H. et al. Large anomalous Nernst effect in thin films of the Weyl semimetal Co_2MnGa . *Appl. Phys. Lett.* **113**, 212405 (2018).

31. Belopolski, I. et al. Discovery of topological Weyl fermion lines and drumhead surface states in a room temperature magnet. *Science* **365**, 1278–1281 (2019).
32. Kerr, J. On rotation of the plane of polarization by reflection from the pole of a magnet. *London, Edinburgh Dublin Philos. Mag. J. Sci.* **3**, 321–343 (1877).
33. Kim, M. H. et al. Determination of the infrared complex magnetoconductivity tensor in itinerant ferromagnets from Faraday and Kerr measurements. *Phys. Rev. B* **75**, 214416 (2007).
34. Kahn, F. J., Pershan, P. S. & Remeika, J. P. Ultraviolet magneto-optical properties of single-crystal orthoferrites, garnets, and other ferric oxide compounds. *Phys. Rev.* **186**, 891–918 (1969).
35. Thouless, D. J., Kohmoto, M., Nightingale, M. P. & denNijs, M. Quantized Hall conductance in a two-dimensional periodic potential. *Phys. Rev. Lett.* **49**, 405–408 (1982).
36. Xiao, D., Chang, M.-C. & Niu, Q. Berry phase effects on electronic properties. *Rev. Mod. Phys.* **82**, 1–48 (2009).
37. Avron, J. E., Osadchy, D. & Seiler, R. A topological look at the quantum Hall effect. *Phys. today* **56**, 38–42 (2003).
38. Heusler Database. <http://heusleralloys.mint.ua.edu/> (2015).
39. Rauch, Tcv, Nguyen Minh, H., Henk, J. & Mertig, I. Model for ferromagnetic Weyl and nodal line semimetals: topological invariants, surface states, anomalous and spin Hall effect. *Phys. Rev. B* **96**, 235103 (2017).
40. Noky, J., Gooth, J., Felser, C. & Sun, Y. Characterization of topological band structures away from the Fermi level by anomalous Nernst measurements. *Phys. Rev. B* **98**, 1–5 (2018).
41. Noky, J., Xu, Q., Felser, C. & Sun, Y. Large anomalous Hall and Nernst effects from nodal line symmetry breaking in Fe_2MnX ($X = \text{P, As, Sb}$). *Phys. Rev. B* **99**, 165117 (2019).
42. Kim, K. et al. Large anomalous Hall current induced by topological nodal lines in a ferromagnetic van der Waals semimetal. *Nat. Mater.* **17**, 794–799 (2018).
43. Miyasato, T. et al. Crossover behavior of the anomalous Hall effect and anomalous Nernst effect in itinerant ferromagnets. *Phys. Rev. Lett.* **99**, 1–4 (2007).
44. Webster, P. J. Magnetic and chemical order in Heusler alloys containing cobalt and manganese. *J. Phys. Chem. Solids* **32**, 1221–1231 (1971).
45. Masumoto, H. & Watanabe, K. New compounds of the Clb, Cl types of RhMnSb , IrMnSn and IrMnAl , New L21 (Heusler) type of Ir_2MnAl and Rh_2MnAl alloys, and magnetic properties. *J. Phys. Soc. Jpn* **32**, 281 (1971).
46. Suits, J. C. Structural instability in new magnetic heusler compounds. *Solid State Commun.* **18**, 423–425 (1976).
47. Kresse, G. & Furthmüller, J. Efficiency of ab-initio total energy calculations for metals and semiconductors using a plane-wave basis set. *Comput. Mater. Sci.* **6**, 15–50 (1996).
48. Perdew, J. P., Burke, K. & Ernzerhof, M. Generalized gradient approximation made simple. *Phys. Rev. Lett.* **77**, 3865–3868 (1996).
49. Suzuki, T. et al. Large anomalous Hall effect in a half-Heusler antiferromagnet. *Nat. Phys.* **12**, 1119 (2016).
50. Manna, K. et al. From colossal to zero: controlling the anomalous Hall effect in magnetic Heusler compounds via berry curvature design. *Phys. Rev. X* **8**, 041045 (2018).
51. Mostofi, A. A. et al. wannier90: a tool for obtaining maximally-localised Wannier functions. *Comput. Phys. Commun.* **178**, 685–699 (2008).
52. Yao, Y. et al. First principles calculation of anomalous Hall conductivity in ferromagnetic bcc Fe. *Phys. Rev. Lett.* **92**, 4 (2004).
53. Ebert, H. Magneto-optical effects in transition metal systems. *Rep. Prog. Phys.* **59**, 1665–1735 (1996).

ACKNOWLEDGEMENTS

This work was financially supported by the ERC Advanced Grant No. 291472 'Idea Heusler', ERC Advanced Grant No. 742068 'TOPMAT', and EC project FET-OPEN No. 829044 'SCHINES'.

AUTHOR CONTRIBUTIONS

J.N. carried out all calculations except the MOKE, analyzed the results, and wrote the manuscript. Y.Z. carried out the MOKE calculations. Y.S. and J.G. supervised J.N. and Y.Z. All authors discussed the results and commented on the paper.

COMPETING INTERESTS

The authors declare no competing interests.

ADDITIONAL INFORMATION

Supplementary information is available for this paper at <https://doi.org/10.1038/s41524-020-0342-5>.

Correspondence and requests for materials should be addressed to Y.S.

Reprints and permission information is available at <http://www.nature.com/reprints>

Publisher's note Springer Nature remains neutral with regard to jurisdictional claims in published maps and institutional affiliations.



Open Access This article is licensed under a Creative Commons Attribution 4.0 International License, which permits use, sharing, adaptation, distribution and reproduction in any medium or format, as long as you give appropriate credit to the original author(s) and the source, provide a link to the Creative Commons license, and indicate if changes were made. The images or other third party material in this article are included in the article's Creative Commons license, unless indicated otherwise in a credit line to the material. If material is not included in the article's Creative Commons license and your intended use is not permitted by statutory regulation or exceeds the permitted use, you will need to obtain permission directly from the copyright holder. To view a copy of this license, visit <http://creativecommons.org/licenses/by/4.0/>.

© The Author(s) 2020